Journal of Southeast University (English Edition) Vol. 42, No. 2, pp. 173-186 June 2026 ISSN 1003-7985

Bearing behavior of six-pile thick pile caps under different reinforcement configurations

DAI Guoliang, SHI Xiangyuan, GONG Zhiyu, GONG Weiming

(School of Civil Engineering, Southeast University, Nanjing 211189, China; Advanced Ocean Institute of Southeast University, Nantong 226010, China)

Abstract: To investigate the bearing behavior and failure modes of six-pile thick pile caps under different reinforcement configurations and explore the optimal reinforcement scheme, this study examined four scaled specimens (S1-S4) with distinct reinforcement designs. The bearing capacity of each pile cap was first calculated using various methods, and laboratory tests were then conducted to determine cracking and ultimate loads. Reinforcement stresses and key strain measurements in the pile caps were monitored, and the crack propagation process was documented in detail. The results demonstrate that the spatial truss model yielded calculations closest to experimental values. Specimen S3 with mesh reinforcement exhibited the highest bearing capacity but required greater steel consumption. The truss-reinforced S4 showed enhanced ductility at failure but posed constructability challenges. Uniformly reinforced S1 delivered the lowest bearing capacity and developed more uneven cracks. Furthermore, a comprehensive analysis of reinforcement stress distribution, internal force flow transfer, and the validity of the plane-section assumption at the pile-cap sides revealed that the mechanical behavior of the six-pile thick pile cap is more closely aligned with the spatial truss model. The concentrated reinforcement scheme at the pile head, as suggested by this model, proves to be an efficient and practical design solution.

Key words: thick pile cap; space truss model; scale model test; numerical simulation; mechanism analysis

DOI: 10. 3969/j. issn. 1003-7985. 2026. 02. 004

The plan dimensions of pile caps, which are widely used as load-bearing foundation components in military, industrial, and civil engineering projects, are determined by the number and arrangement of piles, while their thickness typically increases with higher design bearing capacities. Recent urbanization and advancements in construction techniques have driven the rise of large-scale projects, demanding progressively greater bearing capacities from pile caps. As a result, cap thickness has continuously increased, eventually evolving into block-like structures with similar dimensions in all directions. This complex structural behavior renders the assumptions for flexural members in traditional design codes no longer applicable, and engineering practice has confirmed significant discrepancies between theoretical flexural capacity calculations and actual measured strength [1-3].

To more accurately characterize the load-transfer mechanisms of thick pile caps, a spatial truss model has been proposed and validated through extensive research[4-13]. Based on the 34-pile cap of the Chishi Large Bridge in Hunan Province, He et al. [4] conducted scaled-model tests with varying thicknesses and reinforcement layouts. They found that moderately increasing the cap thickness and concentrating reinforcement in the pile-top region effectively enhances the bearing capacity, while the distribution of pile reaction forces remains relatively unaffected. The applicability of the spatial truss model was validated through complementary finite element analysis. Lu et al. [5] performed scaled model tests (1:5) on six-pile wall-supported caps with five reinforcement arrangements and loading distributions. Their experimental results substantiated that the load-transfer mechanism conforms to the space truss model, where concrete functions as inclined struts and reinforcing bars act as tension members. In their study, the failure modes were primarily characterized by strut splitting or tension rod yielding. Subsequently, Lu et al. [14] extended this research by examining nine-pile, sixteen-pile, and eighteen-pile thick caps, confirmed the suitability of the space truss model for cluster pile cap analysis and systematically evaluated the influence of key parameters, including cap thickness and reinforcement configuration, on the overall bearing capacity. Cavers et al. [15] performed a systematic comparative evaluation of various design methodologies through experimental testing of four-pile cap models. This evaluation revealed that the tension chord design approach specified in the European concrete code yielded predictions most consistent with experimental measurements. Adeber et al. [16] developed an improved design methodology for thick pile caps

Received 2025-06-26, **Revised** 2025-09-16.

Biography: DAI Guoliang (1975—), male, doctor, professor, daigl@seu. edu. cn.

Foundation items: The National Natural Science Foundation of China (No. 52378328, 52208333, 52178317), Research Fund for Advanced Ocean Institute of Southeast University (No. KP202404, GP202403).

Citation: DAI Guoliang, SHI Xiangyuan, GONG Zhiyu, et al. Bearing behavior of six-pile thick pile caps under different reinforcement configurations [J]. Journal of Southeast University (English Edition), 2026, 42(2): 173-186. DOI: 10. 3969/j. issn. 1003-7985. 2026. 02. 004.

based on comprehensive model test analyses. The study recommended concentrating horizontal reinforcement at pile-top locations and proposed adopting the maximum sustainable strut stress as the shear control criterion for thick caps.

However, most existing studies have not systematically documented or analyzed the failure modes and progressive failure mechanisms of thick pile caps. Furthermore, research on the influence of different reinforcement configurations on the load-bearing capacity and failure processes of pile caps remains limited[17-18]. To address the research gaps, this paper investigates the load-transfer mechanism and failure modes of a thick six-pile cap under a column through destructive tests on four differently reinforced models. Combined with theoretical analysis and finite element simulation, the applicability of the flexural model and the spatial truss model for its calculation and design was discussed.

1 Definition of Thick Pile Caps and Associated Calculation Theories

The stress distribution in pile caps is relatively complex and can be broadly interpreted through two design approaches, distinguished by their associated failure modes and mechanisms. The first approach considers pile caps as general flexural members and uses the critical section method to calculate their flexural capacity, as adopted in China's Technical Code for Building Pile Foundations (GB 50007—2011)[19] (hereinafter referred to as the building code), the American ACI code, and the Standard for Structural Calculation of Reinforced Concrete Structures of the Architectural Institute of Japan. The second approach, considering the three-dimensional load-bearing characteristics of thick pile caps, recommends analysis using the strut-and-tie model. This methodology is employed in China's Specifications for Design of Highway Reinforced Concrete and Prestressed Concrete Bridges and Culverts (JTG 3362—2018)[20] (hereinafter referred to as the highway code), Canada's Design of Concrete Structures (CSA A23. 3-04), and Europe's Design of Concrete Structures (EN1992-1-1).

Extensive research[1-5, 9, 14, 21] has demonstrated that thick pile caps deviate from the key assumption in flexural models (plane section assumptions during the initial elastic stage of loading), and the mechanical behavior of these caps is more accurately represented through design and analysis based on the spatial truss theory. In contrast, thin pile caps are primarily dominated by flexural failure, for which the traditional critical section method remains applicable. Therefore, determining whether a pile cap should be classified as "thick" or "thin" is a fundamental prerequisite for appropriate structural design.

1.1 Definition of thick pile caps

Although the criteria for distinguishing between thin and thick pile caps have not yet been fully standardized, the classification is generally determined using the depth-to-span ratio D/h_0 (the linear distance from the calculated perimeter of the column or wall to the farthest pile center relative to the effective depth of the pile cap) and the inclination angle of the compression strut θ (the angle between the diagonal strut and the horizontal plane in the spatial truss model). The calculated perimeter in Fig. 1 is defined using the distance of half the radius from the equivalent perimeter of the column. The equivalent perimeter is calculated according to the following principle: for circular columns, it is equal to the outer circumference; while for rectangular columns or walls, it is calculated based on the principles of maintaining an identical centroid position and an equal outer circumference[2].

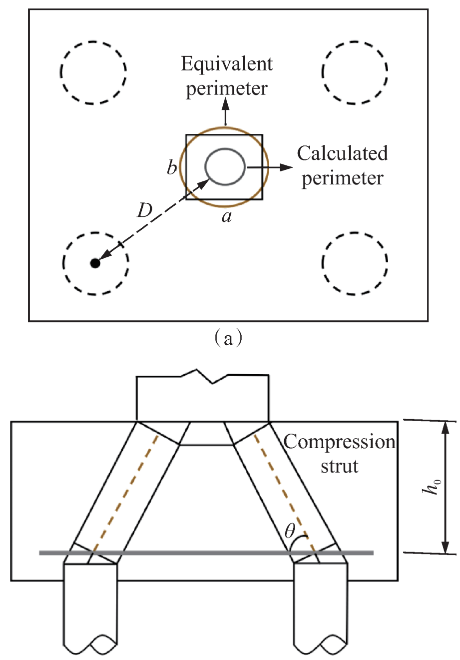

Fig. 1 Span-to-depth ratio and inclination angle of the diagonal strut of the pile cap. (a) Pile cap plan view; (b) Pile cap elevation view

Lu et al.[5] concluded that if the minimum inclination angle θ of any compression strut satisfies $\theta \geqslant \arctan 0.5$, pile cap failure is primarily controlled by strut splitting, and this condition should be met before applying the spatial truss model. Based on experiments and nonlinear finite element analysis of steel fiber-reinforced concrete multipile caps, Sun[22] suggested that when $w/h_0 \geqslant 1$, punching-shear failure dominates, and the spatial truss model is applicable, where w is the horizontal distance from the pile center to the column edge. Guo et al.[2] statistically analyzed extensive test data and proposed that pile caps with $D/h_0 \leqslant 2$ should be defined as "thick"; for such pile caps, the spatial truss model describes structural behavior more accurately than the flexural model.

Several design codes also include relevant provisions regarding this matter. For example, the appendix of the ACI code[23] includes methods for calculating spatial truss models, and it specifies that they can be used for thick pile caps with span-to-depth ratios $D/h_0 \leqslant 2$, which is largely consistent with Lu's conclusions. In contrast, the Canadian standard[24] broadens the application of spatial truss theory by allowing its use whenever the compression strut angles exceed 15°. The highway code[20] is the earliest and only domestic standard to incorporate spatial truss models, permitting strut-and-tie design when the distance from outer-row piles to the pier/abutment edge is less than or equal to the cap height (i. e., strut angles $\theta \geqslant 45°$).

1.2 Calculation theories for pile caps

To verify which computational model more closely aligned with the actual load-transfer mechanism of thick six-pile caps, this study introduced bearing capacity calculation methods from two representative Chinese design codes: the flexural model in the building code and the spatial truss model in the highway code. These two methodologies were applied to the experimental pile cap specimens, and their computational accuracy was assessed against experimental results.

1.2.1 Critical section method

The building code[19] stipulates that pile caps can be calculated as flexural members simplified as beams or slabs. Specifically, separate verifications should be conducted for local bearing capacity, flexural capacity, shear capacity, and punching shear capacity. The punching shear check includes both column punching and corner pile punching. This approach aligns with relevant concrete design codes to ensure sufficient overall load-bearing capacity.

The failure modes of pile caps correspond to these verification items. It is considered that ultimate failure occurs either due to large concrete cracks developing at critical sections—such as the bottom or regions of maximum shear—caused by flexure or shear, or due to the formation of a dislocation mechanism between the column/pile top and the main body of the pile cap resulting from punching shear failure.

1.2.2 Spatial strut-and-tie method

In recent years, an increasing number of national codes have begun to adopt the calculation method based on the spatial truss model for pile caps. The highway code[20] is the first national design standard to adopt this approach in China. It specifies that when the distance between the centerline of outer-row piles and the pier/abutment edge is less than or equal to the pile cap height, the ultimate bearing capacity should be calculated using the strut-and-tie methodology. The concrete at the connection between the bottom of the column (wall) and the center of the pile is usually regarded as a pressure rod, and the steel bar at the connection between the center of the adjacent pile is usually regarded as a tension tie[5-6,17-18,25] (Fig. 2). And the capacity of both the diagonal struts and the ties must be checked simultaneously. The code considers that pile caps fail due to various failure modes derived from the splitting of diagonal struts or the yielding of ties. Additionally, it stipulates that the reinforcement ratio for ties should not be less than 0.15%.

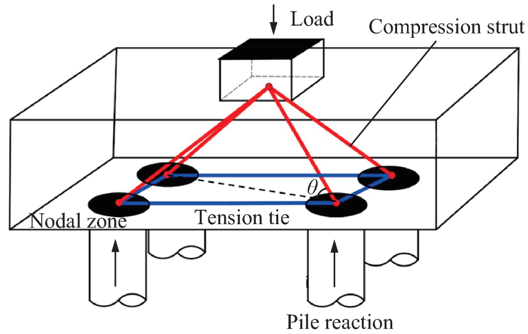

Fig. 2 Spatial truss model of column-supported four-pile cap

Owing to length limitations, the specific calculation formulas are omitted in this paper. Readers may consult building code pages 95-99 and pages 94-96 of the highway code. Fundamentally, both methods can be used to evaluate the maximum bearing capacity at different critical locations (critical sections for the flexural model and strut-tie components for the spatial model), with the minimum value governing the overall pile cap capacity.

2 Model Test

The model test investigated thick six-pile caps with central loading, representing typical prototypes of 1.5-3.0 m thickness at a 1∶5 scale. Geometric similarity was maintained in all dimensions, and the reinforcement ratio was kept consistent in both principal directions. Limited by test conditions and funding, secondary factors were neglected. Observations focused on failure modes and processes of caps, while measurements included cracking load, failure load, cap displacement, and reinforcement stress changes during loading.

2.1 Specimen geometry

As shown in Fig. 3, the model featured a 360 mm thick cap with an effective thickness of 260 mm, the pile diameter was maintained at 180 mm, and the center-to-center spacing was 3.0D (where D denotes the pile diameter); these specifications are in accordance with the minimum spacing requirements of relevant design codes. The supporting column had a cross-section of 220 mm × 220 mm, and the cap's plan dimensions were 2 160 mm × 1 435 mm. The column and piles are 300 mm in height, with vertical structural reinforcement detailed at the bottom of the column and the top of the piles, respectively. Based on the aforementioned criteria, the specimen fell into the thick pile cap category.

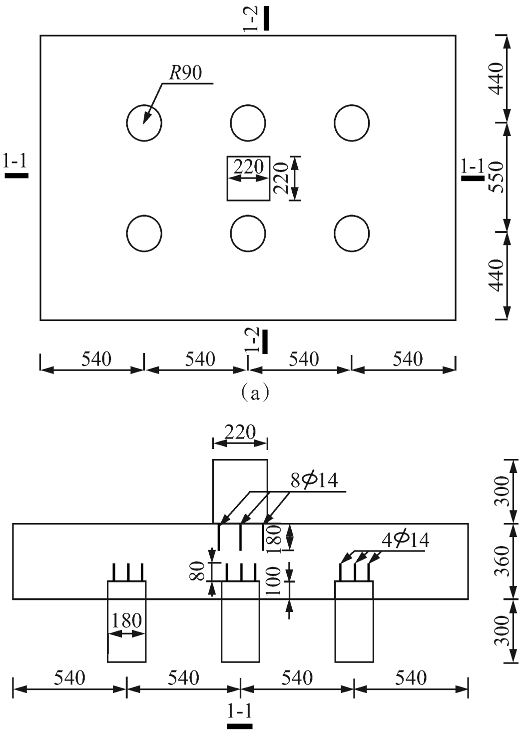

Fig. 3 Specimen dimensions (unit: mm). (a) Plan view; (b) Section 1-1

2. 2 Reinforcement of each specimen

Four pile cap specimens were constructed for this test, and the specimens were numbered S1, S2, S3, and S4.

2. 2. 1 Specimen S1

Specimen S1 incorporated a conventional uniformly distributed reinforcement layout compliant with traditional flexural design specifications. The configuration employed F12 steel bars with a total reinforcement mass of 61. 3 kg, as illustrated in Fig. 4.

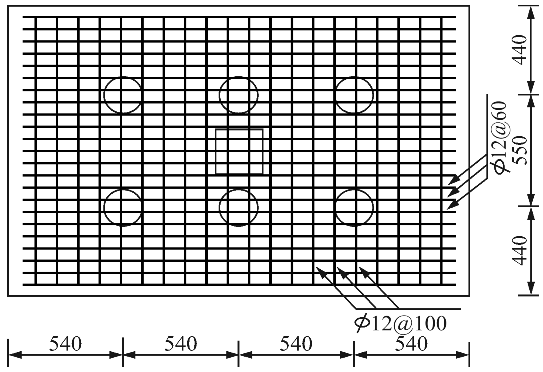

Fig. 4 Uniform reinforcement diagram of S1 (unit: mm)

2. 2. 2 Specimen S2

Specimen S2 featured a modified reinforcement scheme based on the space truss model, with steel bars concentrated above pile locations (Fig. 5) that functioned as tension ties within the truss system. The bar diameter, geometric configuration, and total reinforcement mass (61. 3 kg) were the same as those for Specimen S1.

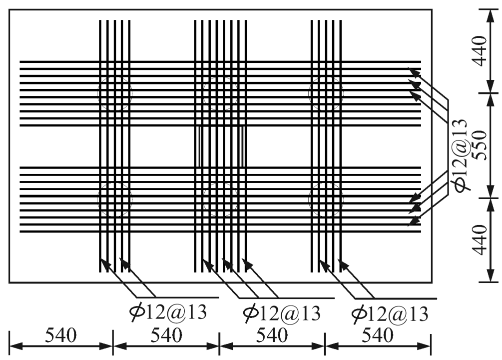

Fig. 5 Centralized reinforcement diagram of Specimen S2 (unit: mm)

2. 2. 3 Specimen S3

Specimen S3 incorporated a multilayered reinforcement configuration comprising four distinct steel meshes. The primary layer replicated the reinforcement pattern of Specimen S2. Superimposed upon this base configuration were three supplementary horizontal reinforcement meshes that were interconnected through vertical reinforcing bars functioning as tension members. The total reinforcement mass measured 92 kg, representing a 50% mass increment compared to Specimen S1 and S2. The complete reinforcement layout and dimensional details are presented in Fig. 6.

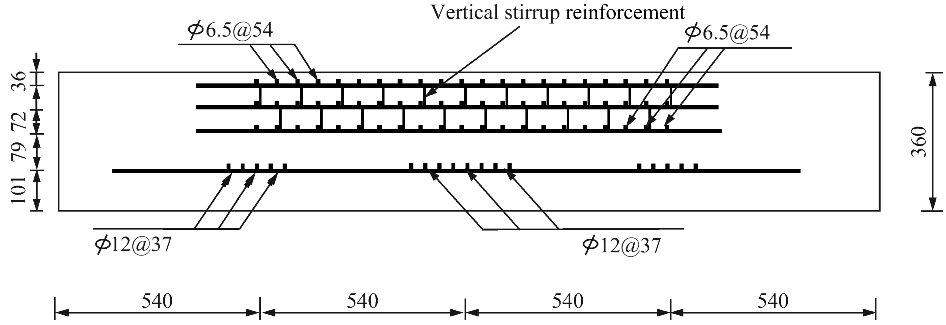

Fig. 6 Four layers of steel mesh reinforcement of S3 (unit: mm)

2.2.4 Specimen S4

Specimen S4 is a steel-truss reinforcement configuration designed based on the assumptions of the spatial truss model. Steel sections were placed at the critical locations of ties and struts within the space truss to fully utilize its excellent tensile and compressive properties, and the section steel utilized comprised 70 mm × 70 mm equal angle steel, with a steel mesh welded onto the base of the spatial truss structure. The total mass of the steel used was 62.8 kg, which was comparable with that of Specimen S1 and S2, as illustrated in Fig. 7.

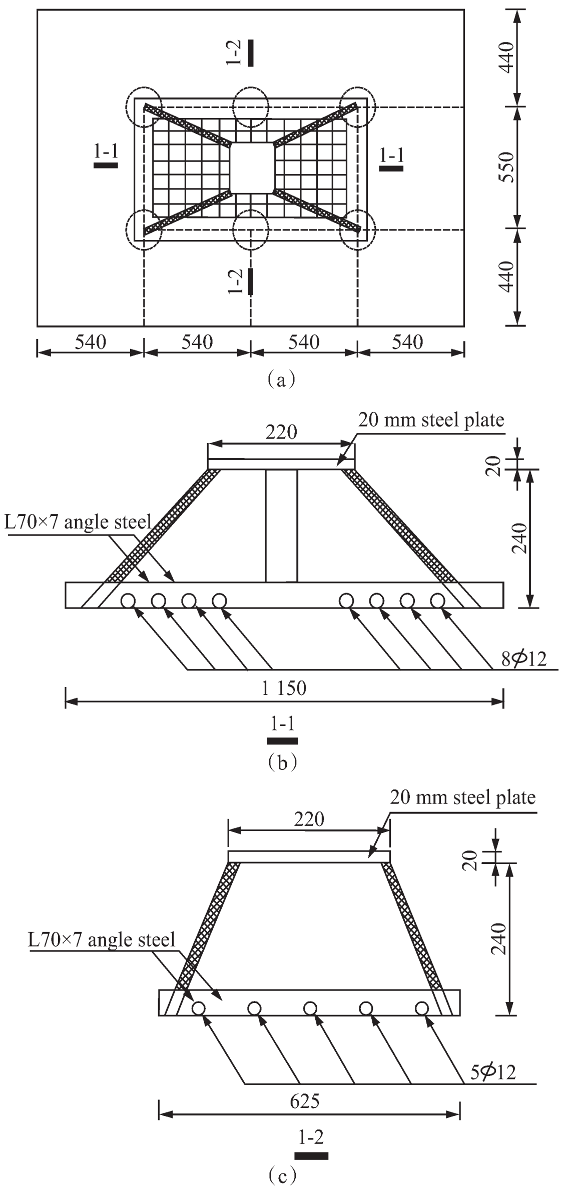

Fig. 7 Truss reinforcement diagram of S4 (unit: mm). (a) Plan view; (b) Section 1-1; (c) Section 1-2

Furthermore, a critical material specification in this experimental program involved the use of C60 high-strength concrete for the pile and column head components and C20 concrete for the slab portion to focus the study on the load-bearing behavior and failure of the slab. The column, piles, and the main body of the pile cap were cast separately. After 28 d of standard curing, they were assembled integrally to ensure structural continuity of the specimen (Fig. 8(a)). The two-way reinforcement was securely tied with iron wires to prevent relative slippage, and it was bent up at the end to enhance the anchorage effect (Fig. 8(b)).

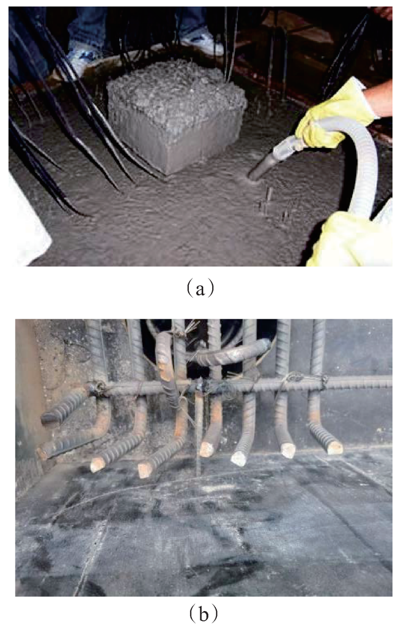

Fig. 8 Pile cap concrete pouring and reinforcement tying. (a) Concrete pouring; (b) Rebar tying and bending operations

2.3 Material property tests and calculations of bearing capacity of pile caps

As shown in Fig. 9, to ensure that the theoretical calculations of the bearing capacity for each pile cap were accurate, and to facilitate subsequent analyses of experi-

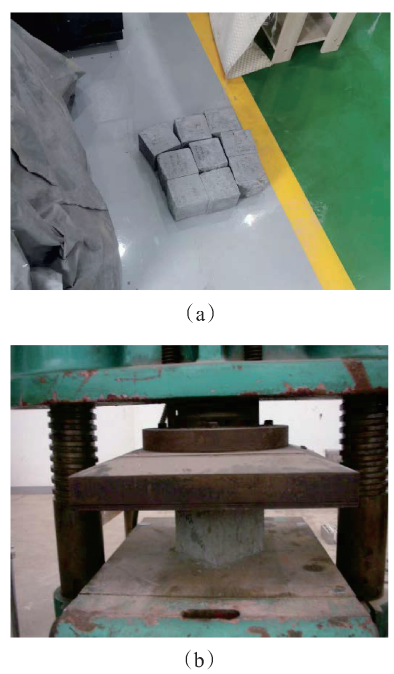

Fig. 9 Concrete property tests. (a) Pre-cast concrete test specimens; (b) Concrete compressive strength test

mental results, material property tests were conducted on the reserved concrete test cubes (after reaching 28 d curing age) as well as on the steel reinforcement. The test results are presented in Tables 1 and 2.

Table 1 Mechanical indices of steel bars and profile steel

Type	Yield tension/kN	Tensile yield strength/MPa	Ultimate tension/kN	Ultimate tensile strength/MPa	Young's modulus/GPa
Rebar(ϕ6.5 mm)	11.6	349	17.1	515	216
Rebar(ϕ12 mm)	35.6	315	52.0	460	192
Profile steel (22 mm×7 mm)	51.7	335	69.5	451	205

Table 2 Mechanical indices of concrete

Pile cap ID	Dimension/(mm×mm×mm)	Compressive failure load/kN	Compressive strength/MPa	Splitting failure load/kN	Splitting tensile strength/MPa	Elastic modulus/GPa
S1	150×150×150	443	19.7	54	1.53	25.6
S2	150×150×150	459	20.4	55	1.56	25.2
S3 (S4)	150×150×150	468	20.8	55	1.56	24.2

The load-carrying capacities of the four specimens were calculated using the flexural model and the spatial truss model. While the flexural model, based on the building code and ACI code, is universally applicable as it ignores complex reinforcement configurations, but the strut-and-tie model in the current code could not be directly applied to Specimens S3 and S4. This is because the contribution of reinforcement mesh and steel profiles to strut capacity cannot be reliably quantified. Guo[26] demonstrated that the web reinforcement in cap enhances both punching capacity and ductility primarily by resisting splitting tensile forces within the web regions of diagonal struts (Fig. 10), and a quantitative calculation formula was further derived:

$$F = S_1 f_{\mathrm{ce(WR)}} = 0.6\pi\left(\frac{D}{2}\right)^2 f_{\mathrm{ce(WR)}} \tag{1}$$

When the bottom longitudinal reinforcement is concentrated in the pile top area,

$$f_{\mathrm{ce(WR)}} = \frac{n\pi \sin\theta A_s \overline{f_y}}{2S_1}\left[\frac{1}{S_2}\left(7.46R + \frac{0.9d}{\sin\theta}\right) + 3.73(\cos\gamma + \sin\gamma)\right] \tag{2}$$

When the bottom longitudinal reinforcement is distributed in a uniform grid,

$$f_{\mathrm{ce(WR)}} = \frac{n\pi \sin\theta A_s \overline{f_y}}{2S_1}\left[\frac{1}{S_2}\left(6.155R + \frac{0.9d}{\sin\theta}\right) + 3.08(\cos\gamma + \sin\gamma)\right] \tag{3}$$

where S_1 is the end surface area of the diagonal strut; $f_{\mathrm{ce(WR)}}$ is the effective compressive strength of the strut in pile caps with horizontal web reinforcement; n is the number of horizontal web reinforcement layers; R is the radius of the strut end surface; d is the effective depth of the pile cap; S_2 is the spacing of bidirectional web reinforcement; A_s is the cross-sectional area of a single bar in

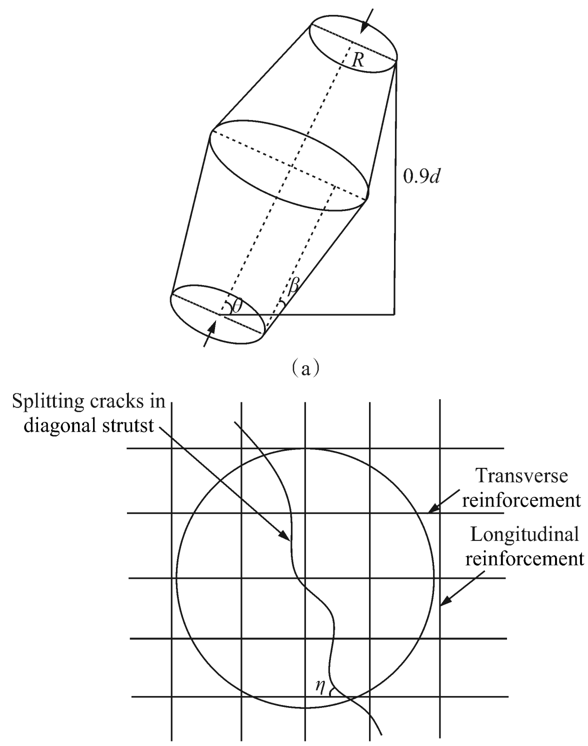

Fig. 10 Splitting forces generated by the mid-region of diagonal struts and horizontal reinforcement mesh[26]. (a) Splitting of inclined strut; (b) Splitting tension of the reinforcement mesh

bidirectional reinforcement; f_y is the yield strength of bidirectional reinforcement; and γ is the angle between transverse web reinforcement and the splitting cracks in the strut web zone.

Therefore, the capacity of S3 can be determined using Eq. (2), and the tie capacity of S4 was calculated using the conventional truss model specified in the code. Furthermore, the four specimens were modeled using the finite element software Abaqus (Fig. 11). The columns, piles, and the main body of the pile cap were modeled using 8-node linear brick (C3D8R) elements with reduced integration. The reinforcement was simulated with truss elements possessing axial stiffness only. The concrete damaged plasticity (CDP) model was adopted for concrete, while a bilinear elastoplastic model was assigned to the steel reinforcement[27-28]. The constitutive parameters for both materials were strictly defined based on the results of the corresponding material property tests. The surface contact conditions at the interfaces of the wall, pile, and cap were defined as a tangential rough and a normal hard contact, and reinforcement bars were embedded within the concrete of the pile cap using an embedded constraint. The boundary conditions included displacement and rotational constraints in the x, y, and z directions at the base of each pile to simulate a fixed pile bottom. A uniform load was applied to the upper surface of the column. The ultimate load was then obtained by loading step by step.

All calculation results are shown in Table 3, where the ultimate bearing capacity of the pile cap within the same method is defined as the lesser of two/three calculated values.

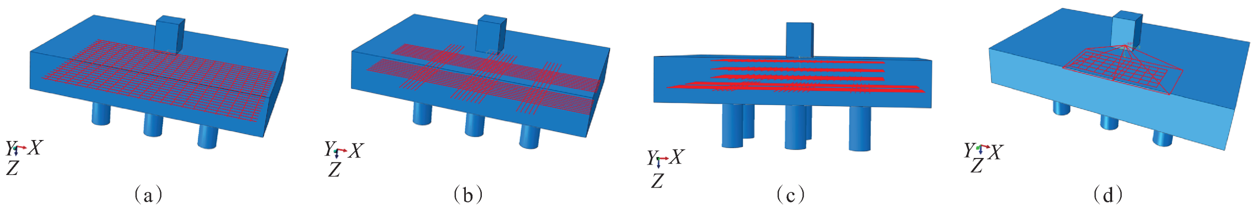

Fig. 11 Abaqus modeling of each pile cap specimen. (a) S1; (b) S2; (c) S3; (d) S4

Table 3 Calculation results of specification kN

Specimen designation		S1	S2	S3	S4
Flexural model (building code)	Shear	936.9	936.9	936.9	936.9
	Punching shear (column)	1 229.2	1 229.2	1 229.2	1 229.2
	Punching shear (corner pile)	1 137.1	1 137.1	1 137.1	1 137.1
Flexural model (ACI)	Shear	1 270.1	1 353.4	1 353.4	1 534.2
	Punching shear	1 437.7	1 437.7	1 437.7	1 437.7
Guo et al's method[2]	Strut compressive capacity			1 780.1	
	Tie tensile capacity			1 755.2	
Spatial truss model	Strut compressive capacity	1 562.5	1 562.5		
	Tie tensile capacity	1 276.6	1 755.2	1 755.2	1 968.6
Numerical simulation		1 150	1 300	1 700	1 550

2.4 Strain gauge arrangement

2.4.1 Deflection variation of cap

A strain gauge was installed at the exact center of the pile cap top surface to monitor variations in vertical deflection under loading. The load-deflection curve of the pier cap can be obtained, thereby evaluating changes in structural stiffness and failure modes.

2.4.2 Failure mode of cap

The fundamental premise of bending theory relies on the plane section assumption. If this assumption is not met during the cap's failure process, the failure mechanism cannot be characterized as flexural. To verify compliance with this assumption, an array of strain gauges was strategically installed along the thickness direction at four critical locations in Fig. 12 to comprehensively capture the strain distribution through the section depth.

2.4.3 Tie of space truss

Sample S1 was selected to study the stress distribution and change in the reinforcement inside the cap, and reinforcement meters were arranged along different paths in

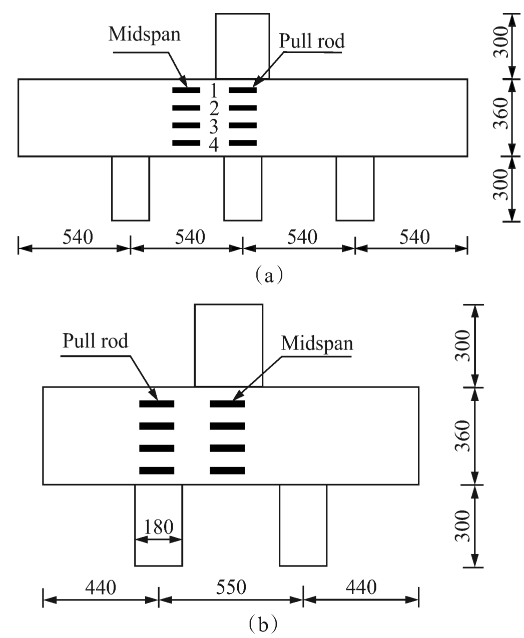

Fig. 12 Position of concrete strain gauge (unit: mm). (a) Long side direction; (b) Short side direction

Fig. 13, including Path A along the long side and Paths B and C along the short side. Path A contained a total of nine reinforcement meters, labeled A1 to A9 from left to right, while Paths B and C had seven reinforcement meters, labeled B1 to B7 and C1 to C7 from top to bottom.

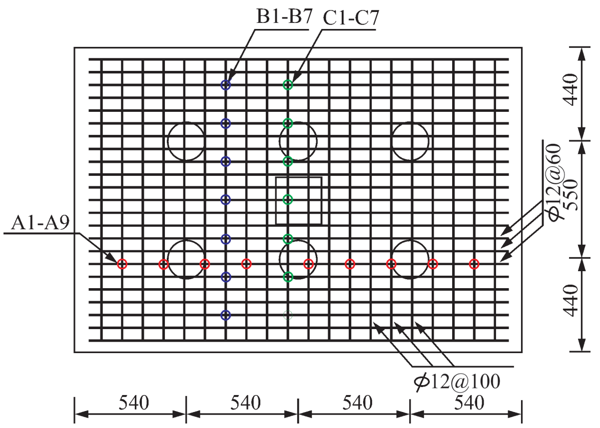

Fig. 13 Layout of reinforcement meter system (unit: mm)

2.5 Test device and loading process

2.5.1 Support and loading device

The experimental setup incorporated a six-pile cap supported by six independently adjustable support units. To facilitate comprehensive crack observation at the cap's soffit, each support was elevated to a height of approximately 1 m. A 320 t hydraulic jack was mounted atop the column head of the test specimen, with a 20 mm thick elastomeric pad inserted at the jack-column interface to ensure uniform load distribution. The loading system was configured such that the jack transferred vertical loads to the reaction frame's bearing table through a rigid distribution beam, maintaining uniaxial loading conditions throughout the test (Fig. 14).

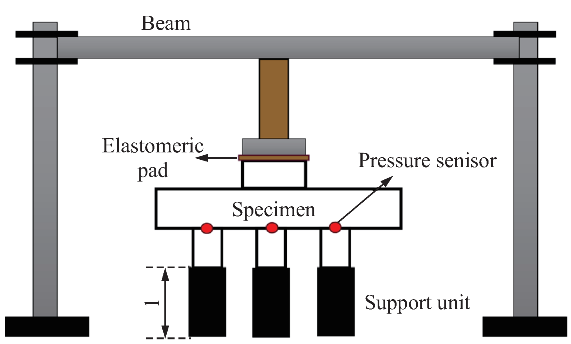

Fig. 14 Loading device of the specimen (unit: m)

2.5.2 Loading mode

Based on preliminary calculations, the estimated cracking load for each specimen was 500 kN. A staged loading protocol was applied, using 50 kN increments up to this load until initial cracking occurred, after which increments were increased to 100 kN. Each stage was held for 15 min to allow stress redistribution and deformation stabilization. As damage accumulated and failure approached, holding time was progressively shortened to continuously monitor failure progression while maintaining complete data acquisition.

3 Test Process and Result Analysis

3.1 Cracking load, failure load, and deflection curve of each specimen

The experimental results revealed distinct failure mechanisms among the test specimens: Specimens S1-S3 consistently exhibited punching shear failure mode, whereas Specimen S4 demonstrated transitional failure behavior from punching shear to flexural failure. The critical performance parameters, including cracking load, ultimate failure load, and maximum midspan deflection, for all four specimens are shown in Table 4, and the load-deflection relationship of the pile cap during the loading process is illustrated in Fig. 15.

Table 4 Test results for each specimen

Specimen	Cracking load/kN	Failure load/kN	Maximum deflection/mm
S1	500	1 250	10.4
S2	500	1 500	9.2
S3	500	1 900	17.2
S4	600	1 700	8.2

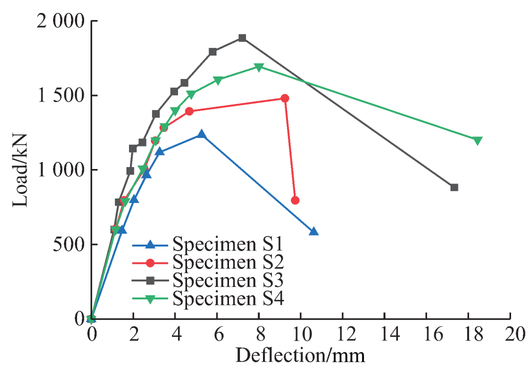

Fig. 15 Load and deflection curves

Due to the mismatch between the uniform reinforcement form of Specimen S1 and the strut-and-tie model, the reinforcement amount in the tension zone of Specimen S1 was significantly lower than that of Specimen S2, which followed the strut-and-tie model. Consequently, the bearing capacity of Specimen S1 was lower, and its stiffness decreased more rapidly compared to Specimen S2. Although the reinforcement ratio of Specimen S4 was similar to that of Specimens S1 and S2, it incorporated section steel in the tension and compression zones of its spatial truss model. This design led to a slower decay in stiffness compared to Specimens S1 and S2, as well as a higher bearing capacity. The reinforcement of Specimen S3 was not only greater than that of Specimens S1, S2, and S4 but also featured three layers of mid-horizontal steel mesh in the web, located precisely in the middle of the diagonal struts. The formation of spatial trusses enhanced its load-bearing capacity by delaying and restricting the splitting and failure of diagonal struts. From the load-deflection curve graph, it can be observed that none of the four caps exhibited obvious turning points upon cracking. Specimens S1, S2, and S3 experienced brittle failure, with the latter dominated by punching failure, but the failure mode of Specimen S4 was primarily characterized by bending failure, and it demonstrated a certain degree of ductility. Based on the comprehensive analysis of the results presented in Table 4 and Fig. 15, it is evident that both the reinforcement configuration and the reinforcement itself significantly influenced the shear failure bearing capacity.

As illustrated in Fig. 16, comparison of the experimental results with the computational results presented in Table 4 shows that the spatial truss model yields the highest computational accuracy, followed by the ACI Building Code. While the ACI Building Code considers only the total reinforcement ratio, it overlooks the influence of reinforcement layout and location. However, for the spatial truss model, only the reinforcement located within the tie zones is considered structurally active. This principle directly explains why, for an identical reinforcement ratio, a pile cap with concentrated reinforcement above the piles demonstrates a higher ultimate capacity than one with reinforcement distributed uniformly across the entire cross-section[4,6,13-14]. Building codes substantially underestimate the structural capacity because they neglect the reinforcement effects, which necessitates increased cap thickness to enhance rigidity and the load-bearing capacity. The calculation method for web reinforcement networks proposed by Guo et al.[2] exhibits the closest agreement with the experimental results of Specimen S3. However, due to constraints imposed by the minimum increment step size in the numerical simulation, the obtained results exhibited systematic underestimations, although a qualitative consistency in behavioral trends was maintained.

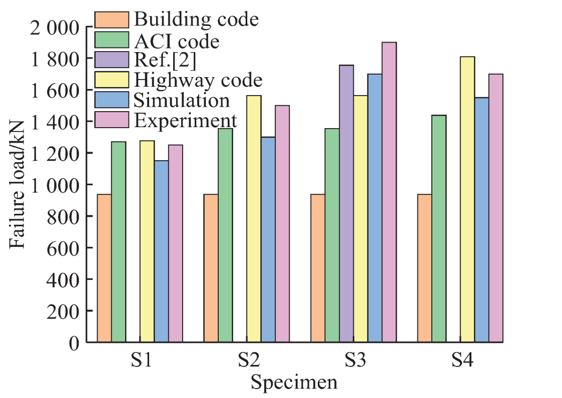

Fig. 16 Comparison between computed and measured values

3. 2 Description of failure process of each cap

To investigate the failure modes and processes of the pile caps, the crack patterns under each load level were recorded and documented.

3. 2. 1 Formation and development of fractures in Specimen S1

Under a loading condition of 500 kN, a curved crack was initiated between the two central piles along the short-side direction and propagated rapidly toward the sides. At 600 kN, in addition to the further extension of the existing short-side crack, a new diagonal crack developed in the midspan region. By 700 kN, the diagonal crack exhibited lateral extension, while the curved cracks along the short side continued their progressive propagation. At 800 kN, a curved crack formed along the long-side direction of the span but demonstrated limited development. Between 1 000 and 1 100 kN, crack development remained gradual. However, at 1 150 kN, the curved fracture within the span underwent rapid extension along the long-side direction, with its ends propagating swiftly toward the sides. Concurrently, radial cracks emerged near each pile, promptly interconnecting to form a punching shear cone, resulting in a decline in jack pressure readings, a sharp increase in deflection, and ultimately, specimen failure. The final damage diagram is shown in Fig. 17. In each crack pattern diagram, the central rectangle represents the bottom surface of the pile cap, Sides ①-④ represent the four developed side surfaces, and Z1-Z6 are the identifiers for the six piles.

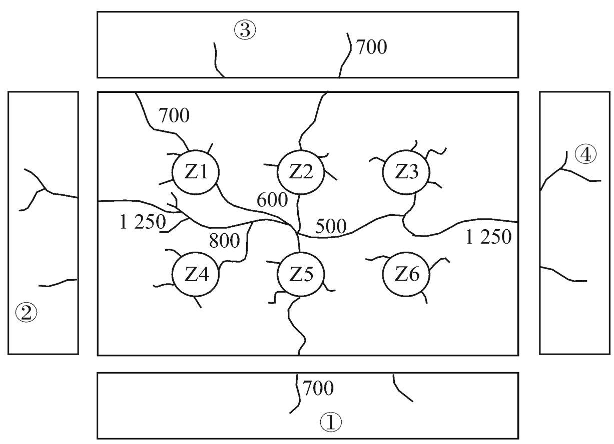

Fig. 17 Fracture diagram of Specimen S1 (unit: kN)

Notably, three splitting cracks were observed around the column head on the roof slab, none of which extended to the plate edge, and no flexural cracks attributable to concrete crushing were detected. Furthermore, no noticeable settlement of the column head was observed. In summary, the failure of the pile cap initiated with the fracture of the inclined struts within the space truss, and it subsequently evolved into punching shear failure.

3. 2. 2 Formation and development of fractures in Specimen S2

When the specimen was subjected to a load of 500 kN, an initial diagonal crack formed within the span. By 650 kN, four radial cracks developed near the initial crack. At 700 kN, these cracks continued to extend, with one crack propagating rapidly toward Side ①. Upon reaching 800 kN, two additional cracks emerged on Side ③, originating from the bottom plate and extending inward, while the remaining cracks showed limited development. At 1 300 kN, nearly simultaneous radial cracks formed adjacent to the four corner piles, all initiating in the midspan region between each pile and the column head without extending to the pile edges. These fractures were attributed to the splitting failure of the inclined struts. By 1 450 kN, these radial cracks propagated toward the pile edges, accompanied by audible cracking sounds and slight dislocation.

At 1 500 kN, the radial cracks around the piles interconnected instantaneously, resulting in a sudden drop in jack pressure, a sharp increase in deflection, and ultimate specimen failure. The concrete along these cracks showed no signs of crushing, nor did the cracks extend to the slab edges. The final damage diagram is shown in Fig. 18. Similar to Specimen S1, these cracks were induced by the splitting failure of the inclined struts. However, compared to Specimen S1, the cracks in Specimen S2 were more uniformly distributed, suggesting that the design of Specimen S2 exhibits superior structural performance relative to Specimen S1.

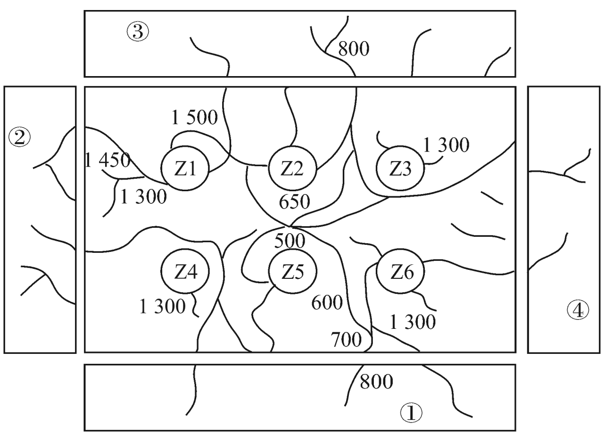

Fig. 18 Fracture diagram of Specimen S2 (unit: kN)

3.2.3 Formation and development of fractures in Specimen S3

Upon reaching 500 kN, a curved flexural crack developed between the piles on both span sides. By 700 kN, two secondary cracks formed at each terminus of the primary crack, oriented diagonally. These cracks extended at 800 kN, circumventing the pile peripheries and propagating toward the lower Sides ③ and ①. At 1 300 kN, the longitudinal curved crack propagated rapidly into the cantilever region. By 1 400 kN, three radial cracks emerged near one pile corner, followed by additional radial cracking on an adjacent pile side at 1 500 kN, while the midspan crack extended toward Sides ④ and ②. Subsequent loading to 1 600 kN caused widening of principal fractures, and at 1 700 kN, radial cracks formed at two additional pile corners. At 1 900 kN, radial cracks initiated at previously uncracked piles, exhibiting rapid width expansion and interconnection to form a punching shear cone, and the concrete spalled downward. The final damage diagram is shown in Fig. 19.

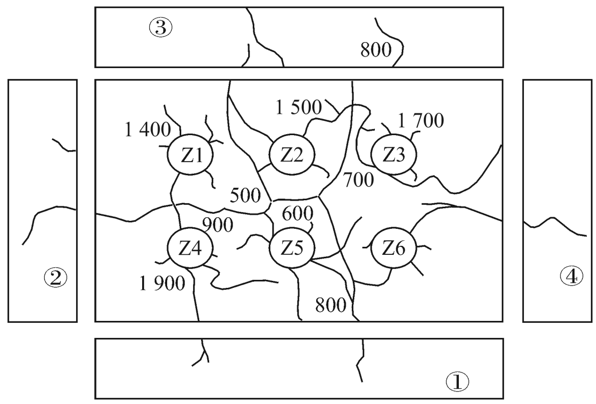

Fig. 19 Fracture diagram of Specimen S3 (unit: kN)

Compared to Specimen S2, the crack distribution of this specimen was more uniform, and it showed superior ductility, which was attributed to the restraint provided by horizontal reinforcement, as this suppressed crack formation. The horizontal reinforcement mesh at the strut mid-depth delayed and confined strut splitting, while the upper-layer reinforcement effectively inhibited flexural cracking. This enhancement significantly improved the bearing capacity of the pile cap.

3.2.4 Formation and development of fractures in Specimen S4

At a load of 600 kN, a curved flexural crack initiated at the midspan of the bottom surface along the short-side direction, propagating approximately 150 mm toward Side ③. When the load increased to 700 kN, this primary crack exhibited both widening and continued propagation along Side ③, while a radial crack developed diagonally from its midpoint, although with limited subsequent development. During the loading phase of 900-1 200 kN, crack propagation essentially stagnated.

Subsequent loading to 1 300 kN caused propagation of the short-side flexural crack toward Side ①, while at 1 400 kN, a new longitudinal crack formed and rapidly extended toward Sides ④ and ②. By 1 500 kN, these cracks exhibited progressive development, culminating at 1 600 kN in the appearance of radial cracks adjacent to each pile edge. Notably, the principal flexural crack at midspan reached a width of 8 mm. Following sustained loading at 1 700 kN for 10 min, the system exhibited pronounced nonlinear behavior characterized by pressure gauge recession and rapid deflection increase to 20 mm, with maximum crack widths reaching 12 mm. The final damage diagram is shown in Fig. 20. The observed damage progression and final failure pattern confirmed the specimen's classification as ductile flexure-punching failure, where the flexural mechanism governed the ultimate limit state.

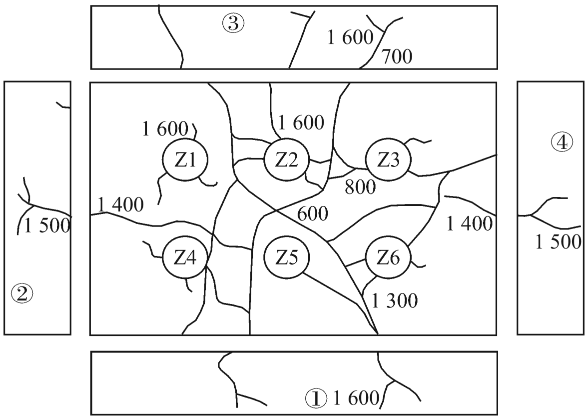

Fig. 20 Fracture diagram of Specimen S4 (unit: kN)

3.3 Reinforcement stress results

Selected readings from each reinforcement meter under a load of 600 kN prior to the cap crack are listed in Fig. 21 in relation to the path, where Path A of the long side is listed separately (Fig. 21(a)), and Paths B and C of the short side are presented together for comparison (Fig. 21(b)). It can be seen that although the overall stress value of the steel bar was small, it was large in the middle and small at the end, and the usual tension characteristics were evident; these results were very similar to the stress of the tie in the space truss model. The stress of the steel bar between piles was obviously greater than the stress on both sides, and the stress between the short side piles was greater than the stress on the long side; moreover, for the two short-side paths, the stress value in Path C was significantly greater than that in Path B. These results indicated that the tensile stress at the bottom of the cap was mainly concentrated in the short side direction, particularly between the two side piles directly below the column.

Based on the overall loading process, the steel stress remained relatively low in the initial stage but exhibited sharp increases at 500 and 1 100 kN, corresponding to the cracking and failure loads of the pile cap, respectively. This demonstrates that the steel and surrounding concrete work compositely to resist tensile forces. As partial concrete cracking and extensive crushing occur, the reinforcement assumes a greater share of the tensile load. This observation indicates that the assumption in the conventional truss model—that ties are entirely composed of reinforcement—is not fully justified.

3.4 Analysis of load-bearing mechanism and failure modes

3.4.1 Analysis of internal stress in pile caps

Previous analyses of sectional stresses in the pile cap and the stresses in reinforcement during testing in this paper have demonstrated that the internal stress distribution in the pile cap follows the pattern predicted by the spatial truss model. Based on the finite element results, a supplementary analysis is now provided to further substantiate this conclusion. Extract iso-stress surface diagrams of each pile cap interior (Fig. 22), it was evident that compressive stresses were predominantly concentrated near the regions between the column base and the pile tops, which corresponded to the concrete compressive struts. The larger iso-stress regions around the two central piles indicated that the pile cap followed the principle of the shortest load-transfer path, with greater compressive stresses aggregated near the pile tops closer to the loading area. The tensile stresses were mainly concentrated at the bottom of the pile cap, particularly between the piles and along the extended lines of the two central piles. The maximum tensile stress occurred between the central piles, which is consistent with the experimental monitoring results.

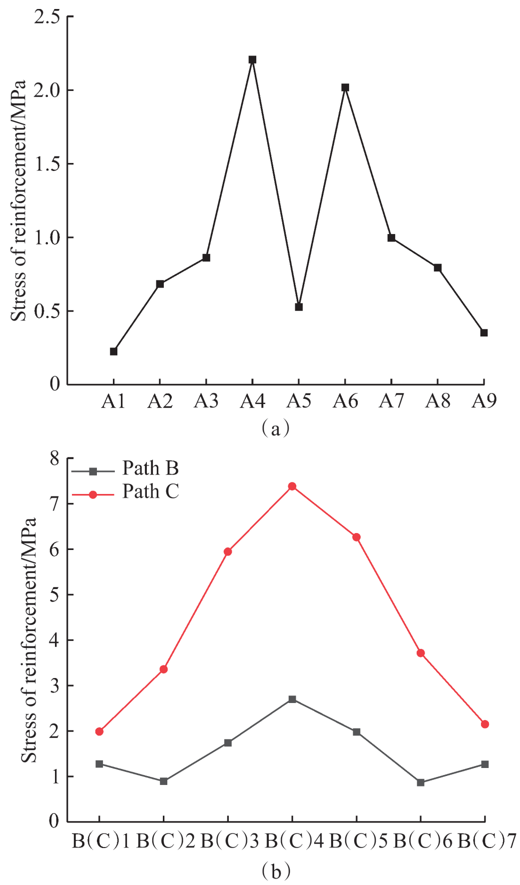

Fig. 21 Stress distribution of reinforcement on different paths. (a) Path A; (b) Paths B and C

The stress tensor symbol diagram (Fig. 23) more intuitively reflects the stress transfer directions of the tensile and compressive members in the spatial truss. Compressive forces were introduced from the column base, concentratedly transmitted through the concrete compressive struts to the piles, with the inclination of most compres-

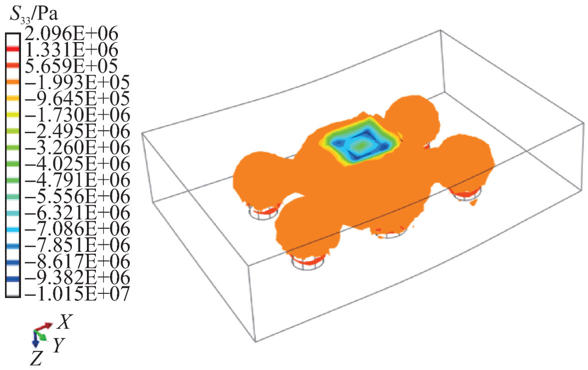

(a)

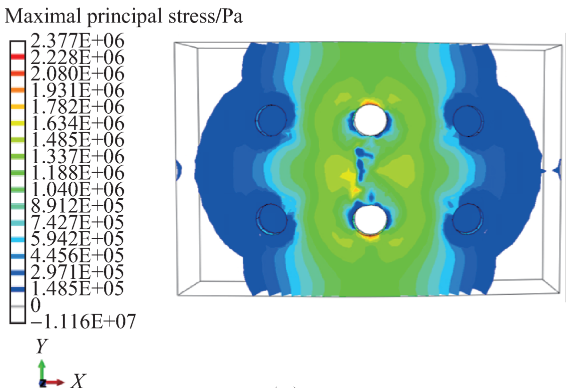

(b)

Fig. 22 Internal iso-surface of stress within the cap. (a) Compressive stress isosurface plot; (b) Tensile stress isosurface plot

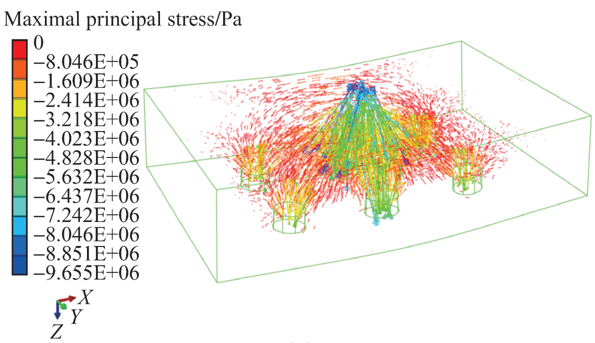

(a)

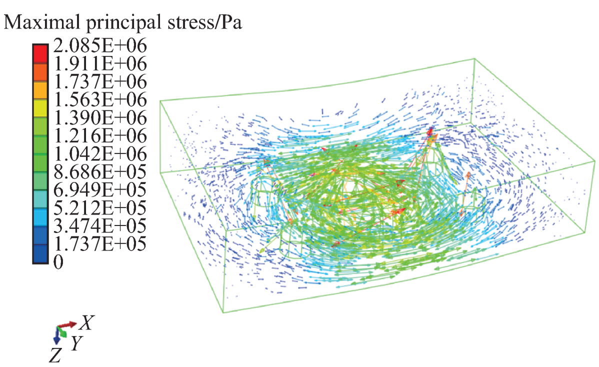

(b)

Fig. 23 Stress tensor symbol plot within the cap. (a) Compressive stress tensor symbol diagram; (b) Tensile stress tensor symbol diagram

sive stress signs generally aligning with the direction of the struts. The tensile forces in the ties were largely oriented along the bottom plane of the pile cap toward the pile tops, serving to provide transverse tension resistance against bottom cracking.

3.4.2 Verification of cap failure mode

Figs. 24 and 25 clearly demonstrate that while the plane-section assumption may have been marginally valid at the midspan between piles (particularly at the cantilevered end), it completely failed to hold true at tie member locations, and the variation in strain did not follow a smooth polygonal pattern. These observations confirmed that the failure mechanism of these thick, heavily reinforced caps did not conform to flexural failure modes, but rather aligned precisely with the predicted failure patterns of the space truss analytical model.

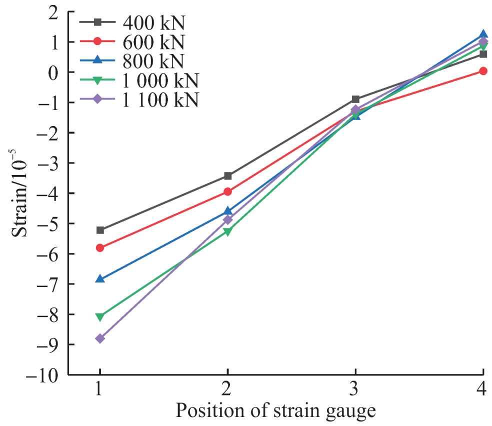

(a)

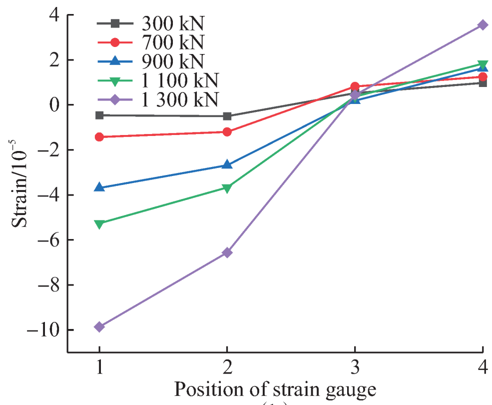

(b)

Fig. 24 Strain of concrete in the middle of the long/short side span along the slab height. (a) Long side; (b) Short side

4 Conclusions

(1) All specimens exhibited similar cracking loads, with failure loads descending in the order of Specimens S3, S4, S2, and S1. However, the web reinforcement network in Specimen S3 required substantially higher reinforcement consumption, and the fabricated steel truss in Specimen S4 involved complex construction. Consequently, the pile-head concentrated reinforcement scheme used in Specimen S2 represents the most practical solution. Comparative analysis showed that the spatial truss model in the Highway Code provided the most accu-

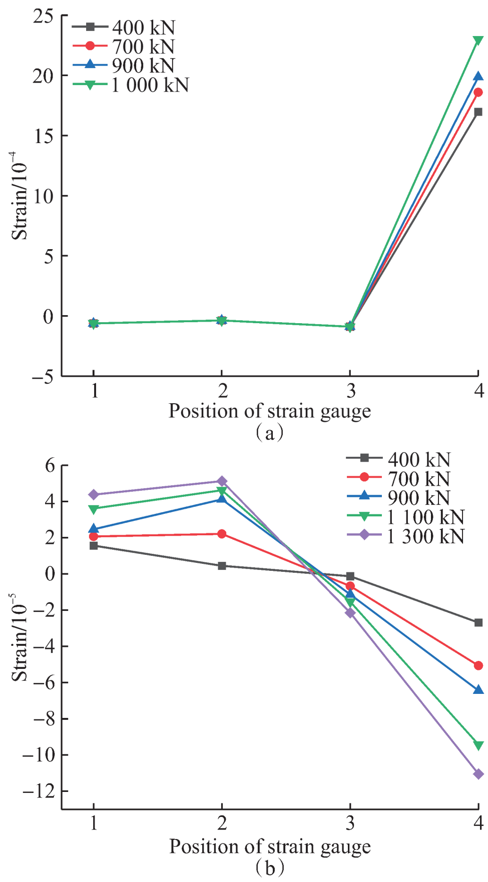

Fig. 25 Strain of concrete at the position of the long/short side tie along the height of the slab. (a) Long side; (b) Short side

rate predictions, while the Building Code showed the poorest agreement due to significant underestimation. Additionally, Guo et al's method achieved the closest correlation with the test results of Specimen S3.

(2) There was no distinct inflection point in the load-deflection curve of each cap. Specimens S1, S2, and S3 exhibited brittle failure, primarily characterized by punching shear failure, whereas Specimen S4 demonstrated a degree of ductility with pronounced bending failure features. During the loading process, the fracture progression and final punching morphology of each cap differed from one another and also deviated from typical flat plate punching behavior. This discrepancy may be influenced by factors such as reinforcement configuration, cap thickness, and pile arrangement.

(3) The stress distribution within the reinforcing steel bars conformed to the theoretical stress distribution of tie members in a spatial truss model, with tensile stresses predominantly concentrated between piles at the bottom of the cap, particularly at the four corners along the shorter sides. Moreover, the stress level remains relatively low prior to cracking, with the concrete contributing a non-negligible tensile resistance. After cracking, the reinforcement stress increases rapidly and spikes again immediately before failure.

(4) Within the pile cap, compressive stresses were concentrated in the region between the column base and the pile heads. The load was transferred from the column base into the cap and converged toward the pile heads through concrete compressive struts. Tensile stresses were concentrated in the plane between piles at the bottom of the cap and oriented laterally toward both sides. Furthermore, the plane-section assumption does not hold throughout loading. These findings collectively indicate that the space truss model offers superior accuracy in capturing the true force transfer mechanism of thick pile caps over the flexural model.

References

[1] SUN G M. Experimental research on thick pile caps of railway bridges [D]. Lanzhou: Lanzhou Jiaotong University, 2014. (in Chinese)

[2] GUO C, GONG W M, LU B, et al. Experimental study on relative stiffness of pile-cap foundation [J]. Chinese Journal of Geotechnical Engineering, 2008, 30(12): 1840-1846. (in Chinese)

[3] LI J X, ZHANG Y Y, LIU X F. Experimental research and theoretical analysis of steel fiber reinforced concrete six-pile double column thick cap [J]. Journal of Building Structures, 2009, 30(2): 149-157. (in Chinese)

[4] HE H N, DAI G L, DIAO Y L. Model test and numerical simulation analysis of space truss with thick cap on large cluster pile foundation [J]. Journal of Civil Engineering, 2015, 48(8): 102-109. (in Chinese)

[5] LU J F, JIANG Y S, LIANG S T. Experimental research on load-carrying properties of six-pile cap under concrete wall [J]. Industrial Construction, 2012, 42(2): 74-77, 32. (in Chinese)

[6] WANG L C, HU L H. Application of strut-and-tie model in design of thick pile cap [J]. Building Structure, 2015, 45(14): 92-98. (in Chinese)

[7] YUN Y M, CHAE H S, RAMIREZ J A. A three-dimensional strut-and-tie model for a four-pile reinforced concrete cap [J]. Journal of Advanced Concrete Technology, 2019, 17(7): 365-380.

[8] SUZUKI K, OTSUKI K, TSUBATA T. Influence of edge distance on failure mechanism of pile caps [J]. Transactions of the Japan Concrete Institute, 2000, 22: 361-365.

[9] ZHOU Y, DAI G L. Parameter study of a new strut-and-tie model for a thick cap with six piles [J]. International Journal of Geomechanics, 2016, 16: B4015005.

[10] SOUZA R, KUCHMA D, PARK J W, et al. Adaptable strut-and-tie model for design and verification of four-pile caps [J]. ACI Structural Journal, 2009, 106(2): 142-150.

[11] ZHAO F Y, JIANG Y S, HOU S M, et al. Field test study on piled raft foundation designed on spatial truss theory [J]. Journal of Southeast University (Natural Science Edition), 2003, 33(5): 597-600. (in Chinese)

[12] SAM C, IYER P K. Nonlinear finite element analysis of reinforced concrete four-pile caps [J]. Computers & Structures, 1995, 57(4): 605-622.

[13] CLARKE J L. Behavior and design of pile caps with four piles: Report 42.489 [R]. London, UK: Cement and Concrete Association, 1973.

[14] LU B, GUO C, GONG W M, et al. Model test study on bearing performance of large caps on cluster piles [J]. Highway, 2008(8): 65-71. (in Chinese)

[15] CAVERS W, FENTON G A. An evaluation of pile cap design methods in accordance with the Canadian design standard[J]. Canadian Journal of Civil Engineering, 2004, 31(1): 109-119.
[16] ADEBER P, KUCHMA D, COLLINS M P. Strut-and-tie models for the design of pile caps: An experimental study[J]. ACI Structural Journal, 1990, 87(1): 81-92.
[17] ABDUL-RAZZAQ K S, FARHOOD M A, JALIL A M. Experimental verification of reinforced concrete pile caps[M]//Proceedings of AICCE'19. Cham, Switzerland: Springer International Publishing, 2019: 879-895.
[18] MATHERN A, CHANTELOT G, SVAHN P O, et al. Enhanced strut-and-tie model for reinforced concrete pile caps[C]//IABSE Reports. Vancouver, Canada, 2017: 607-614.
[19] Ministry of Housing and Urban-Rural Development of the People's Republic of China. Code for design of building foundation: GB 50007—2011[S]. Beijing: China Architecture & Building Press, 2011. (in Chinese)
[20] China Communications Planning and Design Institute Co., Ltd. Specifications for design of highway reinforced concrete and prestressed concrete bridges and culverts: JTG 3362—2018[S]. Beijing: China Communications Press, 2018. (in Chinese)
[21] SONG B, JIN L, DU X L. Experimental study and calculation of shear capacity of FRP-reinforced concrete short beams[J]. Journal of Southeast University (Natural Science Edition), 2024, 54(5): 1080-1088. (in Chinese)
[22] SUN C F. Experimental investigation and nonlinear analysis of thick pile caps[D]. Wuhan: Wuhan University of Technology, 2005. (in Chinese)
[23] American Concrete Institute. Building code requirements for structural concrete: ACI 318-19 and commentary[S]. Los Angeles, CA, USA: ACI Committee 318, 2019.
[24] Canadian Standards Association. Design of concrete structures: CSA A23.3:19[S]. Toronto, ON, Canada: Canadian Standards Association, 2019.
[25] BOULIFA R, SAMAI M L, BENHASSINE M T, et al. Predicting strength capacity of three-dimensional concrete struts in pile caps[J]. ACI Structural Journal, 2021, 118(2): 111-126.
[26] GUO H L. A study of the punching bearing capacity of pile caps under columns with belly horizontal mat reinforcement[J]. China Civil Engineering Journal, 2010, 43(5):79-88. (in Chinese)
[27] SPOZITO R S, RODRIGUES E F C, SANTOS H F, et al. Numerical modeling of four-pile caps using the concrete damaged plasticity model[J]. Buildings, 2024, 14(7): 2066.
[28] DING F X, DENG Y N, WU X. Plastic-damage model and application of confined steel fiber reinforced concrete based on damage ratio strength theory[J]. Journal of Southeast University (Natural Science Edition), 2025, 55(1): 89-97. (in Chinese)

不同配筋形式下六桩厚承台承载特性

戴国亮，史翔元，龚志宇，龚维明

（东南大学土木工程学院，南京 211189；东南大学南通海洋高等研究院，南通 226010）

摘要：为研究六桩厚承台在不同配筋下的承载特性和破坏形式，探讨其最优配筋方案，本文针对4个不同配筋方案的缩尺构件(S1~S4)，首先按不同方法计算各承台承载力，再通过室内试验得到开裂荷载和破坏荷载，同时监测钢筋应力和承台关键处应变，并对各承台的裂缝发展过程进行详细描述。结果表明：空间桁架模型的计算值与试验值更接近；多层钢筋网配筋的S3承载力最高，但耗钢量较多；桁架配筋的S4破坏更具延性，但其实操性较差；均匀配筋的S1承载力最低，且有更多不均匀的裂缝。然后，结合钢筋应力分布规律、承台内部力流传递规律以及承台侧面平截面假定的验证，可知六桩厚承台受力更符合空间桁架模型，模型所建议的桩顶集中配筋是较为经济和便捷的配筋方案。

关键词：桩基厚承台；空间桁架模型；缩尺模型试验；数值模拟；机理分析

中图分类号：TU473.1